machines

MDPI

Article

Vibration Control of Wheels in Distributed Drive Electric Vehicle Based on Electro-Mechanical Braking

Yinggang Xu [1], Zheng Zhu [1], Zhaonan Li [1], Xiangyu Wang [1,2], Liang Li [1,2] and Heng Wei [3,*]

[1] School of Vehicle and Mobility, Tsinghua University, Beijing 100084, China; xuyg21@mails.tsinghua.edu.cn (Y.X.); zhuzheng22@mails.tsinghua.edu.cn (Z.Z.); lzn22@mails.tsinghua.edu.cn (Z.L.); wangxy_15@tsinghua.edu.cn (X.W.); liangl@tsinghua.edu.cn (L.L.)
[2] State Key Laboratory of Intelligent Green Vehicle and Mobility, Beijing 100084, China
[3] School of Automotive and Transportation Engineering, Hefei University of Technology, Hefei 230009, China
* Correspondence: 2025800022@hfut.edu.cn

Abstract

Electro-Mechanical Braking (EMB), as a novel brake-by-wire technology, is rapidly being implemented in vehicle chassis systems. Nevertheless, the integrated design of the EMB caliper contributes to an increased unsprung mass in Distributed Drive Electric Vehicles (DDEVs). Experimental results indicate that when the Anti-lock Braking System (ABS) is activated, these factors can induce high-frequency wheel oscillations. To address this issue, this study proposes an anti-oscillation control strategy tailored for EMB systems. Firstly, a quarter-vehicle model is established that incorporates the dynamics of the drive motor, suspension, and tire, enabling analysis of the system's resonant behavior. The Discrete Fourier Transform (DFT) is applied to the difference between wheel speed and vehicle speed to extract the dominant frequency components. Then, an Adaptive Braking Intensity Field Regulation (ABIFR) strategy and a Model Predictive and Logic Control (MP-LC) framework are developed. These methods modulate the amplitude and frequency of braking torque reductions executed by the ABS to suppress high-frequency wheel oscillations, while ensuring sufficient braking force. Experimental validation using a real vehicle demonstrates that the proposed method increases the Mean Fully Developed Deceleration (MFDD) by 14.8% on low-adhesion surfaces and 15.2% on high-adhesion surfaces. Furthermore, the strategy significantly suppresses 12–13 Hz high-frequency oscillations, restoring normal ABS control cycles and enhancing both braking performance and ride comfort.

Keywords: anti-lock braking system; electro-mechanical braking; vibration; distributed drive electric vehicle

check for updates

Academic Editor: Farshid Naseri

Received: 16 July 2025
Revised: 14 August 2025
Accepted: 15 August 2025
Published: 17 August 2025

Citation: Xu, Y.; Zhu, Z.; Li, Z.; Wang, X.; Li, L.; Wei, H. Vibration Control of Wheels in Distributed Drive Electric Vehicle Based on Electro-Mechanical Braking. *Machines* **2025**, *13*, 730. https://doi.org/10.3390/machines13080730

Copyright: © 2025 by the authors. Licensee MDPI, Basel, Switzerland. This article is an open access article distributed under the terms and conditions of the Creative Commons Attribution (CC BY) license (https://creativecommons.org/licenses/by/4.0/).

1. Introduction

With the rapid advancement of automotive technologies in electrification, intelligent control, lightweight design, and system integration, brake-by-wire technologies have garnered significant attention within the industry [1,2]. Among these, Electro-Mechanical Braking (EMB) systems have emerged as a promising solution due to their high control precision, fast response speed, improved linearity, and higher level of integration. EMB technology is currently undergoing rapid iterations and vehicle-level testing [3,4].

However, compared to conventional hydraulic calipers, EMB units are typically heavier, which increases the unsprung mass of the vehicle. In addition, most test vehicles

equipped with EMB systems adopt a distributed drive architecture, commonly utilizing in-wheel or wheel-side motors integrated with gear reduction mechanisms. These motors are rigidly coupled to the wheels, eliminating the need for a traditional clutch system [5]. As a result, the increased unsprung mass introduced by the EMB system, along with the damping characteristics of the electric motor, alters the natural frequency of the wheel-end system. Real-vehicle data acquisition has shown that wheel speed frequently exhibits abnormal oscillations with a cycle of approximately 75 to 90 ms [6,7]. During braking, such high-frequency wheel speed fluctuations can be easily triggered, leading to repeated torque reductions under ABS intervention. This not only degrades braking performance and extends stopping distances, but also increases the potential risk of severe traffic accidents [8]. Therefore, the implementation of targeted control strategies to suppress high-frequency wheel speed oscillations is essential for ensuring the effective operation of ABS in distributed drive vehicle architectures.

Experimental observations indicate that vibration frequencies associated with high-frequency wheel speed oscillations typically fall within the 10–30 Hz range [9], while disturbances induced by rough or uneven road surfaces are generally irregular and less predictable. Recent research on ABS performance under such conditions has predominantly concentrated on road surface classification and adaptive pressure modulation strategies aimed at minimizing braking force degradation. V. Ciupe et al. utilized a scaled experimental test rig to investigate the impact of uneven road surfaces on ABS braking performance. Their findings revealed that a vertical disturbance of 46 mm led to a notable reduction in braking efficiency and a corresponding increase in stopping distance [10]. Sven Mayer et al. reported that specific uneven surfaces, such as speed bumps, reduced system interaction accuracy by up to 19%, thus impacting the driving experience [11]. Li et al. proposed a sliding mode controller for slip ratio regulation, leveraging wheel speed characteristics under rough road conditions. Their approach effectively reduced braking distance by 4.65 m [12]. Yu developed a hydraulic ABS test platform and implemented a wheel speed correction strategy combining high-pass filtering with a threshold-crossing count method, effectively suppressing abnormal pressure drops under rough road conditions [13]. Nico A. evaluated ABS performance on Belgian pavé road surfaces using Bosch control algorithms and observed vibration phenomena at approximately 100 Hz in SUV tires [14].

In addition to uneven road surfaces, electric motors themselves represent a significant source of wheel vibration in distributed drive vehicles. Zhao identified three primary approaches to mitigate vibration issues in in-wheel motor systems: structural optimization of the motor design, enhancement of control strategies, and the incorporation of supplementary suspension components [15]. Yu Mao investigated the origins of 50–100 Hz vibrations in single-wheel systems equipped with in-wheel motors. Through detailed modeling and analysis, he attributed the vibrations to torque ripple, compounded by the bidirectional rotational dynamics between the hub and the motor, and proposed corresponding optimization strategies to mitigate these effects [16].

The motor can mitigate partial vibration conditions, but when the tire is worn or the damping characteristics of the suspension change over a long period, the vibration will reappear [17], especially when the motor is not involved in the working condition of the brake. Therefore, it is more appropriate to solve the problem by the brake control method. Based on the EMB architecture, this paper proposes a control strategy to identify and suppress the wheel shaking. The main innovations and contributions of this paper are summarized as follows:

- To investigate the origin of tire resonance in distributed drive systems, an integrated tire–motor–suspension dynamic model is established.

- The vibration behavior of in-wheel motors is affected by multiple factors, including unsprung mass, suspension stiffness, tire stiffness, and motor damping. The circumferential vibration of in-wheel motors is primarily influenced by unsprung mass and motor damping.
- The wheel speed oscillation characteristics are extracted, and the inherent resonance frequency of the tire is identified by using the Discrete Fourier Transform (DFT). Analysis reveals that the fundamental resonance frequency of the tire lies within the range of 12.1 to 12.8 Hz.
- A model-based predictive and logic threshold control (MP-LC) strategy for ABS is proposed to actively suppress wheel vibrations.

The structure of this paper is organized as follows: Section 2 presents the single-wheel mathematical model of the distributed drive system and analyzes the underlying resonance mechanisms, highlighting the effects of unsprung mass, motor damping, and suspension stiffness as key parameters influencing the natural characteristics of the tire. Section 3 introduces a vibration frequency identification method and a control strategy designed to suppress resonance. Section 4 analyzes the resonance behavior, revealing that wheel speed fluctuations primarily originate from torsional vibration, with minimal correlation to vertical oscillations. Section 5 describes low-friction ABS simulations conducted using a co-simulation platform combining CarSim and Simulink, along with real-vehicle experiments. The results demonstrate that the proposed algorithm effectively reduces wheel-end vibrations and enhances braking performance. Finally, Section 6 provides the concluding remarks and outlines potential directions for future research.

2. Single-Wheel Model for Distributed Drive Vehicles

A single-wheel dynamic model is developed to analyze the variations in wheel rotational speed during braking, as illustrated in Figure 1. The Basic Wheel Caliper (BWC) functions as the actuator component of the Electro-Mechanical Brake system, receiving braking commands from the Electro-Mechanical Brake Controller (EMBC) via CAN communication. During braking events, the wheel primarily experiences three forces: vertical load, braking torque transmitted through the disc, and longitudinal resistance exerted by the ground [18].

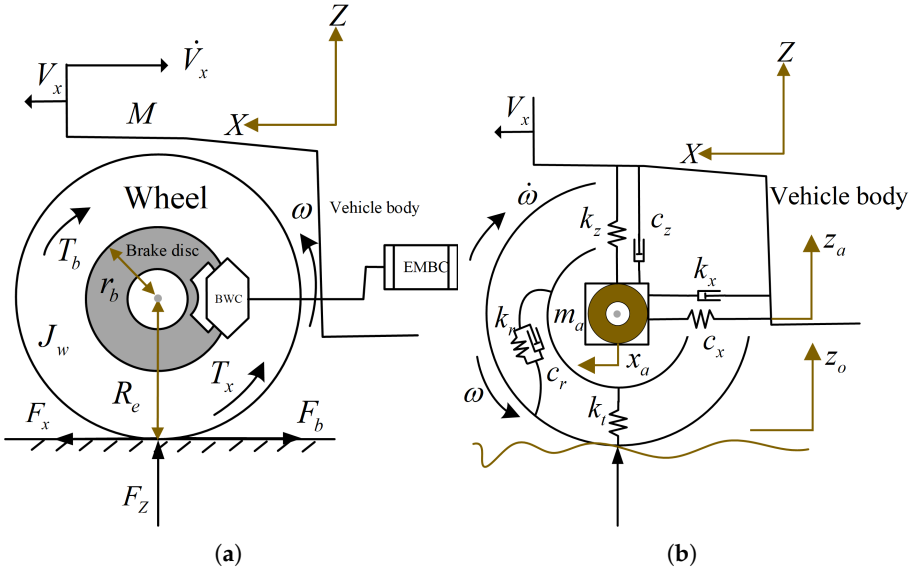


Figure 1. Quarter tire model: (**a**) Tire braking model. (**b**) Tire suspension model.

In parallel, a tire damping characteristic model is constructed to examine the effect of vertical load on wheel speed during braking, as illustrated in Figure 1. The vehicle is modeled as a two-mass system, partitioned into sprung and unsprung masses connected via a suspension assembly composed of springs and dampers [19]. Furthermore, the interface between the tire and the motor is represented as an elastic coupling, capturing the compliance introduced by the motor–tire interaction.

This study hypothesizes that the elastic coupling between the motor and tire is a primary factor contributing to wheel speed oscillations. All parameters utilized in the model are summarized in Table 1.

Table 1. Variables for barking and suspension dynamic models.

Variable	Description	Unit	Variable	Description	Unit
M	Sprung mass	kg	$\dot{\omega}$	Wheel angular acceleration	deg/s^2
m_a	UnSprung mass	kg	T_b	Braking toruqe	Nm
$\dot{V}_x$	Braking acceleration	m/s^2	T_x	Friction Torque	Nm
V_x	Vehicle speed	m/s	r_b	Braking disc radius	m
R_e	Wheel effective rolling radius	m	ω	Wheel angular speed	deg/s
F_x	Friction force	N	k_t	Tire stiffness in vertical Dir	N/m
F_z	Total wheel load	N	k_z	Suspension stiffness in vertical Dir	N/m
F_b	Braking force	N	c_z	Damping coefficient in vertical Dir	Ns/m
z_0	Road excitation	N	k_r	Suspension stiffness in Rotational Dir	N/rad
z_a	Vertical displacement	m	c_r	Damping coefficient in rotational Dir	Ns/rad
x_a	Longitudinal displacement	m	k_x	Suspension stiffness in longitudinal Dir	N/m
J_w	Wheel moment of inertia	kgm^2	c_x	Damping coefficient in longitudinal Dir	Ns/m

2.1. Tire Dynamics Model

According to vehicle dynamics theory, the vehicle dynamics during braking can be expressed by the following equation:

$$M\dot{V}_x(t) = -\mu(\lambda)F_z(t) \tag{1}$$

where λ denotes the longitudinal slip ratio of the wheel, and $\mu(\lambda)$ represents the utilized adhesion coefficient, i.e., the friction coefficient between the tire and the road surface as a function of the slip ratio λ [20]. The wheel dynamics during braking can be described by the following equation:

$$J_w\dot{\omega}(t) = \mu(\lambda)R_eF_z(t) - 2\mu_b r_b F_b(t) \tag{2}$$

where μ_b is the friction coefficient between the brake pad and the disc. r_b is the effective braking radius of the disc. $F_b(t)$ is the normal force applied by the on the brake disc. This force is typically calculated by multiplying the braking pressure by the effective contact area. The factor of 2 accounts for the two-sided clamping force applied to both sides of the disc.

Accordingly, the vertical load can be calculated from Equation (2) as follows:

$$F_z(t) = \frac{J_w\dot{\omega}(t) + 2\mu_b r_b F_b(t)}{\mu(\lambda)R_e} \tag{3}$$

The longitudinal slip ratio of the wheel can be defined by the following set of equations:

$$\lambda = \frac{V_x - R_e \cdot \omega}{\max(|V_x|, \varepsilon)} \tag{4}$$

where ε is a small regularization term introduced to prevent division by zero at low speeds. The variation in wheel load is calculated using Equation (3) as follows:

$$\Delta F_z(t) = \frac{J_w \ddot{\omega}(t) + 2\mu_b r_b \Delta F_b(t)}{\mu(\lambda) R_e} \tag{5}$$

From the perspective of full vehicle dynamics, the vertical load acting on a wheel comprises both a static component and a dynamically transferred component. The dynamic load transfer is primarily caused by the vehicle's longitudinal acceleration during braking or traction events as follows [21]:

$$\begin{cases} F_{zf}(t) = \dfrac{mg(b - h_g \dot{V}_x)}{2L} \\ F_{zr}(t) = \dfrac{mg(a + h_g \dot{V}_x)}{2L} \end{cases} \tag{6}$$

where h_g denotes the height of the vehicle's center of gravity from the ground, a is the distance from the center of gravity to the front axle, and b is the distance from the center of gravity to the rear axle. $F_{zf}(t)$ represents the total vertical load on a single front wheel at time t, while $F_{zr}(t)$ represents the total vertical load on a single rear wheel at time t.

2.2. Tire Model for Suspension Dynamics

A single-wheel suspension dynamics model, illustrated in Figure 1b, is developed in this study. The model is based on a MacPherson independent suspension configuration and incorporates an air spring as the primary elastic element. The vibration characteristics of the wheel are analyzed in three degrees of freedom: vertical (Z-axis), longitudinal (X-axis), and rotational about the Y-axis (circumferential direction). For each degree of freedom, the respective elastic and damping properties are explicitly considered to accurately capture the dynamic behavior of the system.

Among the three directions, variations in stiffness and damping along the longitudinal axis are relatively minor and therefore exert limited influence on the overall wheel vibration behavior. Both experimental measurements and simulation results indicate that the dominant contributors to wheel vibration are the vertical and circumferential modes, with the circumferential mode having a particularly significant impact on the stability of the wheel speed signal.

Based on the above analysis, it is concluded that the jitter observed in the wheel speed signal is primarily induced by the circumferential vibration of the wheel as follows [22,23]:

$$\begin{cases} M\ddot{z}_2 + c_z(\dot{z}_2 - \dot{z}_1) + k_z(z_2 - z_1) = Mg \\ m_a\ddot{z}_1 - c_z(\dot{z}_2 - \dot{z}_1) - k_z(z_2 - z_1) + k_t(z_1 - z_0) = m_a g \\ l_y\ddot{\theta}_a + c_r\dot{\theta}_a + k_r(\theta_a - \theta_b) = -R_e F_b \end{cases} \tag{7}$$

Road tests have shown that electric vehicles (EVs) are more susceptible to wheel vibration than traditional internal combustion engine vehicles [24]. This tendency can be attributed to two primary factors. First, the structural characteristics of electric drivetrains, where the motor inherently introduces damping-like behavior, alter the system's dynamic response. Second, EVs often employ air springs or low-stiffness suspension systems to improve ride comfort, which increases the dynamic compliance of the suspension and consequently heightens the wheel's sensitivity to circumferential vibrations [25].

By analyzing the internal force distribution within the tire model and its associated dynamic differential equations, the total force acting on the wheel can be decomposed into a static load component and a dynamic load component. This relationship can be expressed as follows [26]:

$$F_z(t) = F_{z,st}(t) + F_{z,dyn}(t) \tag{8}$$

$$\begin{cases} F_{z,st}(t) = m_a g \\ F_{z,dyn}(t) = -k_t(z_1 - z_0) \end{cases} \tag{9}$$

where $F_z(t)$ represents the total vertical load acting on the wheel at time t, $F_{z,\mathrm{st}}(t)$ denotes the static vertical load under equilibrium conditions, and $F_{z,\mathrm{dyn}}(t)$ is the dynamic load variation, which arises primarily from the vehicle's longitudinal acceleration and road surface excitation.

Accordingly, the dynamic differential equation governing the suspension system can be reformulated as follows:

$$m_a \ddot{z}_1 = F_{kb} + F_{cb} + F_{z,st}(t) + F_{z,dyn}(t) \tag{10}$$

where F_{kb} represents the bulk elastic force, while F_{cb} denotes the damping force generated by the damper, which is a function of the piston velocity in the variable damping system. Accordingly, the variation in vertical load at the wheel end can be expressed as follows:

$$\Delta F_z(t) = m_a \ddot{z}_1 - (F_{z,st}(t) + F_{z,dyn}(t)) \tag{11}$$

By analyzing Equation (11), the natural (resonant) frequency of the tire system can be derived. Based on the variation in vertical force and the corresponding motion equations, it becomes evident that the masses m_a (unsprung mass) and M (sprung mass) are dynamically coupled, contributing to the system's vibrational behavior.

- If the unsprung mass m_a is assumed to be stationary (i.e., $z_1 = 0$), the system simplifies to a single-degree-of-freedom undamped vibration model for the sprung mass. The corresponding natural circular frequency is given by the following equation: $\omega_0 = \sqrt{k_1/M}$
- Conversely, if the sprung mass M is considered stationary (i.e., the vehicle body does not move), and the unsprung mass m_a is allowed to vibrate freely, the system again behaves as a single-degree-of-freedom undamped oscillator. The resulting natural circular frequency is as follows: $\omega_t = \sqrt{(k_1 + k_t)/m_a}$
- In the analysis of rotational (circumferential) motion, the system can be modeled such that the tire provides torsional stiffness, while the damping torque is primarily introduced by the electric motor. The motor's damping effect is represented by a viscous damping coefficient k_r, which defines the relationship between the damping torque and the angular velocity. When the electric motor is back-driven by the wheel during braking, the coupled rotational system—comprising the tire and motor—exhibits a characteristic natural frequency. Assuming a simplified single-degree-of-freedom torsional vibration model, this natural circular frequency can be expressed as follows: $\omega_r = \sqrt{k_r/m_a}$

In practical applications, the vibration frequency of the vehicle body is substantially lower than that of the wheel—typically by a factor of approximately 1/100. Moreover, to simplify the computation and satisfy the constraints of real-time execution on the embedded brake controller, the model is deliberately streamlined. Consequently, this analysis focuses exclusively on the vibration of the tire (unsprung mass), while the dynamic influence of the vehicle body (sprung mass) is neglected for simplification.

Under this assumption, the vertical dynamics of the tire can be simplified and expressed [27] as follows in Equation (12):

$$m_a\ddot{z_1} + k_c\dot{z}_1 + (k_1 + k_2)z_1 - k_t z_0 = F_z \tag{12}$$

According to vehicle dynamics theory, the vertical amplitude–frequency response of the sprung mass (z_1) relative to the road excitation (q) can be derived. The amplitude ratio z_1/q, as a function of excitation frequency, reveals a resonance behavior determined by the system's stiffness and mass properties. The corresponding analytical expression is given in Equation (13):

$$\left|\frac{z_1}{q}\right| = \gamma\left[\frac{(1-\beta^2)^2 + 4\zeta^2\beta^2}{\Delta}\right]^{\frac{1}{2}} \tag{13}$$

In this context, the term Δ is defined in Equation (14), where $\gamma = \frac{k_2}{k_1}$ denotes the stiffness ratio, and $\mu = \frac{m_1}{m_2}$ represents the mass ratio, $\beta = \omega/\omega_0$ represents the frequency ratio.

$$\Delta = \left\{(1-(\omega/\omega_0)^2)\left[1+\gamma-\frac{1}{\mu}(\omega/\omega_0)^2\right]-1\right\}^2 + 4\zeta^2(\omega/\omega_0)^2\left[\gamma-\left(\frac{1}{\mu}+1\right)(\omega/\omega_0)^2\right]^2 \tag{14}$$

The natural frequency of the simplified vertical vibration system is given by the following equation: $\omega_t = \sqrt{(k_1+k_t)/m_a}$, and the corresponding damping ratio is expressed as follows: $\zeta_t = \frac{k_c}{2\sqrt{(k_1+k_t)m_a}}$.

In the circumferential (rotational) direction, the natural frequency and damping ratio are respectively defined as follows: $\omega_\theta = \sqrt{K_r/J}$ and $\xi_\theta = \frac{k_r}{2\sqrt{k_r J}}$.

The damping coefficient of the motor primarily arises from the back electromotive force (EMF) generated during rotation. This electromagnetic damping effect can be approximated by the following expression: $k_c = \frac{9.55\cdot k_e^2}{R_a}$, where k_e is the motor back EMF constant, and R_a is the armature resistance.

To facilitate analysis of the system's frequency response characteristics, the circumferential dynamic equation (Equation (8)) is transformed into the frequency domain using the Fourier Transform.

$$\theta_a(-l_y\omega^2 + jc_r\omega + k_r) = \theta_b * k_r \tag{15}$$

The variable ξ_b can be interpreted as the ratio of vehicle speed to wheel radius. This formulation is primarily introduced to highlight the influence of the slip ratio on tire dynamics. When the slip ratio remains within a relatively small range, the longitudinal force generated at the tire–road interface can be reasonably approximated as being linearly proportional to the slip ratio. Accordingly, the slip ratio serves as a key parameter characterizing the longitudinal force transmission between the tire and the road surface [28]. Based on this, the frequency-domain transfer function of the system can be expressed as Equation (16).

$$H(j\omega) = \frac{\theta_a}{\theta_b} = \frac{k_r}{-l_y\omega^2 + jc_r\omega + k_r} \tag{16}$$

By introducing the frequency ratio γ and the damping ratio ξ, the frequency-domain transfer function can be reformulated in a normalized form, as shown in Equation (17).

$$H(j\omega) = \frac{1}{1-\beta^2 + 2j\xi\beta} \tag{17}$$

3. Model Prediction Logic Threshold Control (MP-LC) and Adaptive Braking Intensity Field Regulation (ABIFR)

The overall control logic is illustrated in Figure 2. Based on a single-wheel dynamic model, the inherent characteristics of the tire are analyzed, and the actual resonance frequency is identified using empirical data. A model-based prediction of wheel speed variation is then performed, and an adaptive torque reduction strategy is integrated to regulate the final braking force.

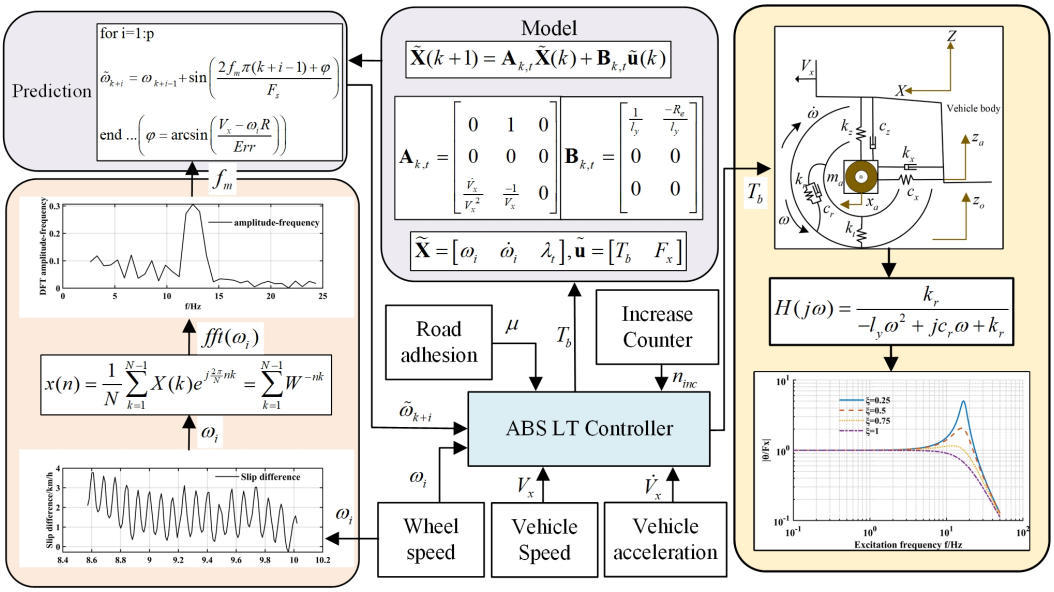


Figure 2. Overall logic block diagram.

3.1. Model Prediction

This study proposes a hybrid control strategy that integrates logical threshold-based decision-making with a model-based predictive framework to detect and forecast wheel vibration phenomena. Specifically, when an abnormal slip ratio is identified—such as a condition where the braking force is relatively low while the slip ratio remains unexpectedly high, often indicative of self-excited wheel oscillations—the controller suppresses the conventional torque reduction response. Instead, it sustains or incrementally increases the braking force to maintain braking effectiveness and ensure system stability.

According to the prediction model, by differentiating Equation (4), the value of $\Delta\lambda$ can be obtained. The relationship between the slip ratio at the current time step and that at the subsequent time step is expressed by Equation (18) [29].

$$\lambda(k+1)=\begin{bmatrix}\frac{R_e\omega(k+1)}{V_x^2(k+1)} & \frac{-R_e}{V_x(k+1)}\end{bmatrix}*\begin{bmatrix}\Delta V_x(k+1)\\ \Delta\omega(k+1)\end{bmatrix}+\lambda(k) \tag{18}$$

$$V_x(k+1)=V_x(k)+\dot{V}_x(k)T_s \tag{19}$$

$$\omega(k+1)=\omega(k)+\dot{\omega}(k)T_s \tag{20}$$

Accordingly, the control-oriented state-space equations can be formulated as shown in Equation (21).

$$\tilde{\mathbf{X}}(k+1)=\mathbf{A}_{k,t}\tilde{\mathbf{X}}(k)+\mathbf{B}_{k,t}\tilde{\mathbf{u}}(k) \tag{21}$$

where $\mathbf{A}_{k,t} = \begin{bmatrix} 0 & 1 & 0 \\ 0 & 0 & 0 \\ \frac{\dot{V}_x}{{V_x}^2} & \frac{-1}{V_x} & 0 \end{bmatrix}$, $\mathbf{B}_{k,t} = \begin{bmatrix} \frac{1}{l_y} & \frac{-R_e}{l_y} \\ 0 & 0 \\ 0 & 0 \end{bmatrix}$, $\tilde{\mathbf{X}} = \begin{bmatrix} \omega & \dot{\omega} & \lambda \end{bmatrix}$, $\tilde{\mathbf{u}} = \begin{bmatrix} T_b & F_x \end{bmatrix}$.

The slip ratio λ is obtained from Equation (4), which can be calculated directly from the vehicle speed and wheel speed. Based on the current state of the vehicle, the predictive model estimates the evolution of the slip ratio over the next N_p sampling intervals. To regulate the wheel slip ratio $\lambda(k)$ towards its optimal value—thereby maximizing road adhesion and braking efficiency—the desired braking torque is determined in accordance with the road–tire friction characteristics.

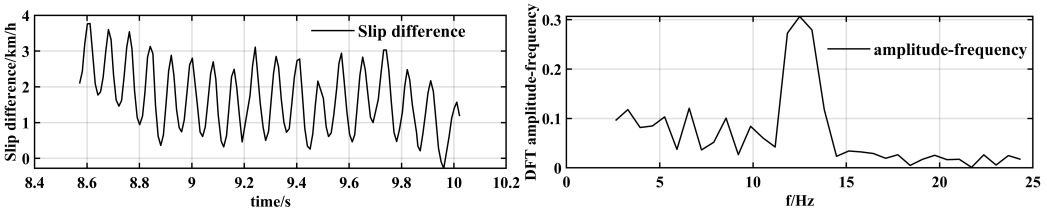
Using Equation (21), future values of wheel speed and vehicle speed over a prediction horizon of N_p steps can be forecast based on historical wheel speed data, current road adhesion conditions, and the actual braking force. By employing the EMB caliper, the clamping force can be measured with high accuracy, enabling precise calculation of the braking torque T_b. In this study, F_x is considered as the longitudinal resistance, which primarily consists of aerodynamic drag and rolling resistance.

In addition, the vehicle's resonance characteristics should be taken into account. A Fourier Transform is performed on the wheel speed data over a past time window of at least 80–90 ms to extract the wheel's inherent rotational characteristics. By identifying the spectral peak, the resonance frequency can be determined [30].

$$X(k) = \sum_{k=1}^{N-1} x(n) e^{-j\frac{2\pi}{N}nk} (k = 1, 2, 3 \ldots N-1) \tag{22}$$

where $X(k)$ represents the DFT transformed data, $x(n)$ is the sampled analog signal, and N is the total number of sampling points. For the signal with a period of 80 ms, the sampling frequency is 5 ms once, there are 16 data points in total, and at least 8 points are enough to ensure the accuracy [31]. In this paper, N = 150 is selected.

The results of the Fourier Transform are shown in Figure 3. A segment of the wheel speed and vehicle speed deviation is extracted and analyzed using a DFT, revealing a consistent frequency component f_m in the range of 12–13 Hz. Extensive testing on the M917 vehicle—over 100 datasets—confirmed this observation, with no significant oscillations detected at other frequencies. Therefore, the peak resonance frequency can be identified either online in real time or offline and calibrated into the control algorithm for a specific vehicle. Furthermore, by applying the inverse Fourier Transform, the original time-domain signal can be reconstructed based on the identified natural frequency.



(**a**) (**b**)

Figure 3. High-frequency wheel speed oscillation and Fourier analysis: (**a**) Extracted vehicle speed and wheel speed deviation. (**b**) Frequency spectrum obtained from Fourier Transform.

$$x(n) = \frac{1}{N} \sum_{k=1}^{N-1} X(k) e^{j\frac{2\pi}{N}nk} = \sum_{k=1}^{N-1} W^{-nk} \tag{23}$$

Therefore, the predicted oscillatory wheel speed over the future time horizon from step k to $k + N_p$ is given by the following equation:

$$\tilde{\omega}_{k+i} = \omega_{k+i-1} + A_m \sin(2f_m \pi(k + i - 1) + \varphi) \tag{24}$$

where φ denotes the phase angle, which can be calculated as follows: $\varphi = \arcsin((V_x - \omega R_e)/A_m)$. During each torque reduction event, the phase is corrected and set to $\pi/2$. A_m is the amplitude. Even for special road surfaces such as cobblestone, the same phase reset strategy during each torque reduction is necessary to prevent multiple unnecessary interventions. During ABS braking, the wheel-speed oscillation can be approximated by a sinusoid. Each time the wheel speed reaches its minimum, the ABS reduces torque; in a sinusoidal representation, this event corresponds to a phase of $3\pi/2$. To counteract this, the wheel-speed compensation term is designed to be quadrature to the oscillation—i.e., with a phase of $\pi/2$—so that the two signals complement each other and attenuate the oscillatory component.

In cases of sudden road surface transitions—e.g., from asphalt to ice—the detection cycle is typically around 100 ms, and the processing cycle is approximately 300 ms. This corresponds to a control algorithm operating at a different frequency band.

3.2. Adaptive Braking Intensity Field Regulation

To mitigate excessive torque reduction during braking, an Average Braking Intensity Field strategy is proposed. The vehicle's average deceleration during braking reflects the spatiotemporal evolution of braking intensity under current road adhesion conditions. Based on this intensity field, a reasonable lower bound for torque reduction is established to prevent over-intervention, thereby enhancing both braking stability and efficiency [32].

The braking strength $z(t)$ is given by the ratio of the braking force $F_b(t)$ of the vehicle to the vertical load $F_z(t)$: $z(t) = F_b(t)/F_z(t)$. The average braking strength $\bar{z}(t)$ represents the braking state in the past period (window width T):

$$\bar{z}(t) = \frac{1}{T} \int_{t-T}^{t} z(\tau) d\tau \tag{25}$$

Based on the current braking intensity, the upper and lower bounds of the allowable braking force can be estimated. Torque reduction is permitted only when the torque increase over a past time window is significant, the current wheel deceleration lies within the stable range, and the actual braking force approaches its estimated upper bound. Otherwise, the reduction in torque is suppressed proportionally to the difference between the actual braking force and its lower bound, in order to prevent excessive braking force attenuation.

Accordingly, the lower bound of the braking intensity is defined as $z_{min}(t) = \alpha z(t)$, where $\alpha \in [0.6, 0.7]$ reflects a safety margin. The current braking force is denoted by $F_b(t)$, and the minimum allowable braking force under torque reduction is given by $F_{b,low}(t) = z_{min}(t) Fz(t)$. The cumulative torque increase over a specified past time interval and is calculated as follows:

The final target torque reduction can be written as follows:

$$\Delta F_b^{\text{up}}(t) = \int_{t-T}^{t} \max\left(0, \frac{dF_b(\tau)}{d\tau}\right) d\tau \tag{26}$$

The final target torque reduction can be written as follows:

$$F_b^{\text{target}}(t) = \max\left(F_{b,\text{low}}(t), F_b(t) - \beta \cdot \Delta F_b^{\text{up}}(t)\right) \tag{27}$$

3.3. Increase/Decrease in Overall Brake Force of ABS

The ABS control algorithm based on estimated braking force is illustrated in Figure 4. This algorithm evaluates the wheel's operating condition—whether it lies within the stable or unstable region—by analyzing the slip ratio and wheel deceleration. The boundary conditions defining the unstable region are shown in the figure, where the horizontal axis represents wheel acceleration, and the vertical axis represents the slip ratio.The test vehicle used in this study was the Mengshi 917, manufactured by Dongfeng Motor Corporation, Wuhan, Hubei Province, China. The vehicle was equipped with electro-mechanical brake (EMB) calipers supplied by Jonyi Automotive Co., Ltd., Suzhou, Jiangsu Province, China. The experimental tests were conducted on wetted tile surfaces and asphalt pavement. When the slip ratio–wheel deceleration point lies above the unstable boundary, the wheel is considered to be in an unstable state. Conversely, when the point is below the stable boundary, the wheel is regarded as being in the stable region. During ABS operation, when the wheel enters the stable region, the braking force is increased; conversely, when the wheel enters the unstable region, the braking force is reduced.

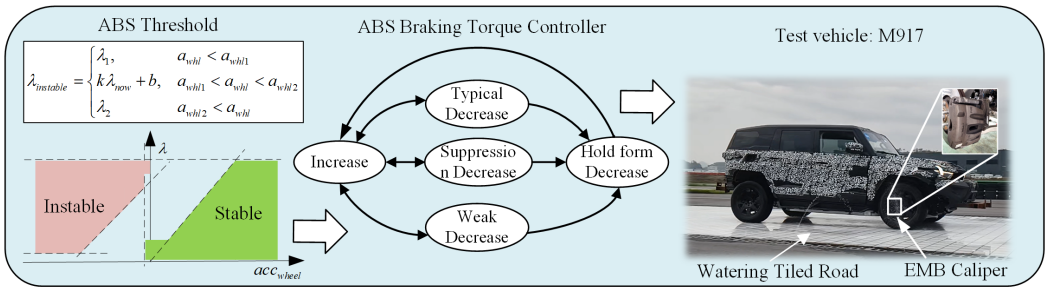


Figure 4. ABS controller and test vehicle.

$$\lambda_{instable} = \begin{cases} \lambda_1, & a_{whl} < a_{whl1} \\ k\lambda_{now} + b, & a_{whl1} < a_{whl} < a_{whl2} \\ \lambda_2, & a_{whl2} < a_{whl} \end{cases} \tag{28}$$

where λ_1, λ_2 represent two slip rate threshold values, and a_{whl} represents wheel acceleration.

Normal torque reduction is permitted only when the vehicle's previously averaged braking potential energy is sufficient, the cumulative increase in braking torque is adequate, and the MP-LC prediction confirms that the current decrease in wheel speed is due to normal deceleration rather than resonance-induced oscillations. If the torque increase is insufficient, the system applies a moderated torque reduction—referred to as a weak decrease—based on the ABIFR. During torque reduction, the MP-LC method resets the phase component of the oscillatory wheel speed to zero and monitors the actual wheel speed oscillation over the subsequent 80 ms. If abnormal oscillations are detected, further torque reduction is suppressed.

By integrating a logic-threshold-based control approach, the slip ratio of the tire is maintained within an optimal range of approximately 5% to 15%. This range is known to correspond to the maximum achievable longitudinal tire force. This strategy ensures the effective utilization of tire–road friction, thereby improving overall braking performance under varying operating conditions.

4. Wheel Vibration Characterization and Frequency Spectrum Analysis

To validate the proposed theory, all algorithms were verified through full-scale vehicle tests using M917, with a total mass of 3.8 t. The vehicle was equipped with EMB calipers on all four wheels, with the front calipers providing a braking force range of 0–65 kN and the rear calipers 0–45 kN. The algorithms were deployed on the S32K344 microcontroller,

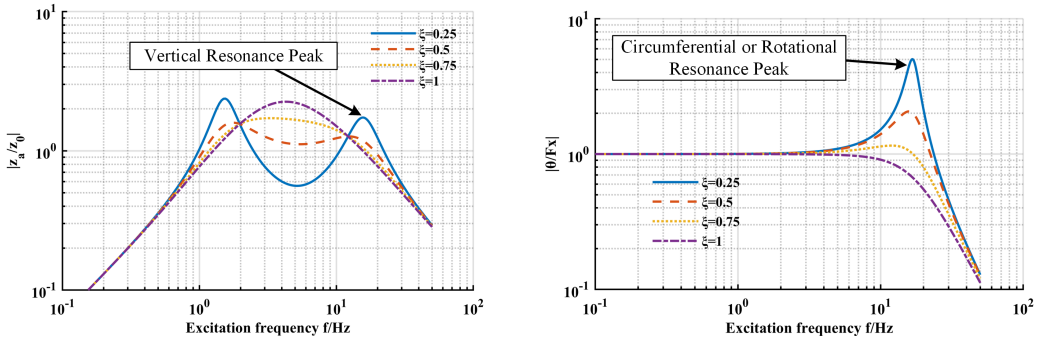
featuring a 300 MHz processing capability, manufactured by NXP Semiconductors, Eindhoven, the Netherlands, and data acquisition was performed using a ZLG-CANFD device, manufactured by Guangzhou Zhoulizgong Electronics Co., Ltd., Guangzhou, China. All tests were conducted in spring at the Huanggang Proving Ground in Hubei. The high-adhesion surface consisted of dry asphalt with an adhesion coefficient of approximately 1.0, while the low-adhesion surface was a water-sprayed tile road with an adhesion coefficient of 0.1–0.2.

In the single-wheel system model, the vehicle body mass is set to 1000 kg, the wheel mass to 100 kg, the suspension stiffness to K = 100,000 N/m, and the tire stiffness to kt = 900,000 N/m. The damping coefficient C varies within the range of 5000 to 20,000 N·s/m. Four damping ratios are analyzed: 0.25, 0.5, 0.75, and 1.0. The resulting vertical vibration frequency response of the tire is illustrated in Figure 5a, where the transfer function from ground excitation z_0 to tire vertical displacement z_a is evaluated.

The results indicate that when the damping ratio is below 0.5, two distinct resonance peaks emerge. The low-frequency resonance near 1–2 Hz has minimal impact on tire dynamics, whereas the resonance observed in the 10–20 Hz range significantly influences the tire's response. Suspension height sensor data indicate vertical vibrations occur below 2 Hz, ruling out vertical dynamics as the source of high-frequency tire oscillations.

The 1–2 Hz low-frequency components, however, align well with the measured suspension height variations, supporting this interpretation.

Figure 5b illustrates the frequency response characteristics of the wheel's rotational motion with respect to circumferential force. When the damping is low, a resonance peak tends to appear around 10–11 Hz, which aligns well with the resonance frequency observed in the experimental data in Figure 3.



(**a**) (**b**)

Figure 5. Frequency domain characteristic diagram of tire system: (**a**) Vertical vibration Bode plot of dual mass system. (**b**) Bode diagram of tire circumferential vibration.

A high-speed camera was employed to focus on the wheel during braking in order to investigate its oscillation characteristics. The objective was to determine whether the source of the vibration originated from vertical, lateral, or circumferential motion. Given that the observed wheel speed oscillation period is approximately 80 ms, the Nyquist sampling theorem requires a sampling interval shorter than half the period—at least 25 Hz (i.e., one sample every 40 ms). The video was recorded in 4× slow motion, and 8 frames were extracted per second, resulting in an effective sampling frequency of 32 Hz, which satisfies the Nyquist criterion.

As shown in Figure 6, The numbers 1–16 indicate the chronological order of captured frames. The consecutive frames recorded during braking reveal no observable vertical displacement of the tire relative to the vehicle body, suggesting that vertical oscillation is unlikely to be the primary cause.

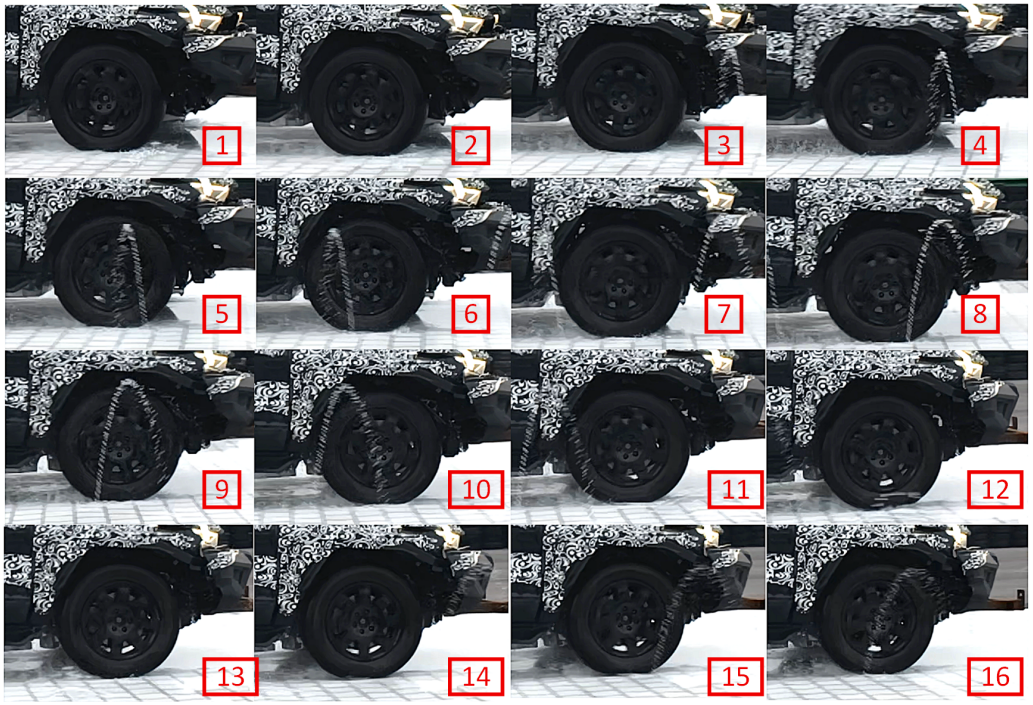


Figure 6. Single wheel vibration under ABS condition (capture frequency of 32 frames per second).

ABS and TCS tests were conducted using the M917 vehicle on a simulated low-adhesion surface (water-sprayed ceramic tiles). As shown in Figure 7a,c,e, in the braking scenario, braking was initiated at 65 s. The wheel speeds rapidly decreased, triggering ABS intervention to maintain the wheel slip ratio within 5–15%. A high-frequency oscillation was observed in the left front wheel, with a period of approximately 80 ms. Since no suppression control was applied, the braking torque also exhibited a passive torque reduction at the same frequency (80 ms), fluctuating between 1000 and 3000 N. In contrast, the right rear wheel exhibited a normal ABS cycle of around 300 ms, with braking torque ranging between 0 and 4000 N. Analysis of the suspension height data from CASS (Controller of Air Suspension System) for both the left front and right rear wheels revealed no oscillation at 80 ms intervals; instead, the suspension vibrations occurred at much lower frequencies (300–500 ms). This indicates that there is no direct correlation between suspension vertical displacement and high-frequency wheel speed oscillation.

In the traction scenario as shown in Figure 7b,d,f, throttle input was applied at 46.3 s, triggering immediate TCS intervention. The driving torque fluctuated between 300 and 400 Nm. From 51 to 56 s, large slip ratios and oscillations were observed, with frequencies around 12 Hz. The driving torque, influenced by the wheel speed signals, also exhibited an 80 ms oscillation pattern. Both driven wheels displayed high-frequency vibrations, which were clearly perceptible to the occupants as strong chassis vibrations, leading to a noticeable degradation in ride comfort. However, suspension height data revealed no high-frequency oscillation, only normal low-frequency movement.

In summary, based on both suspension height measurements and high-speed video observations, it is concluded that the observed chassis vibrations are not caused by vertical motion of the wheels but are primarily attributed to circumferential (rotational) oscillations of the wheels.

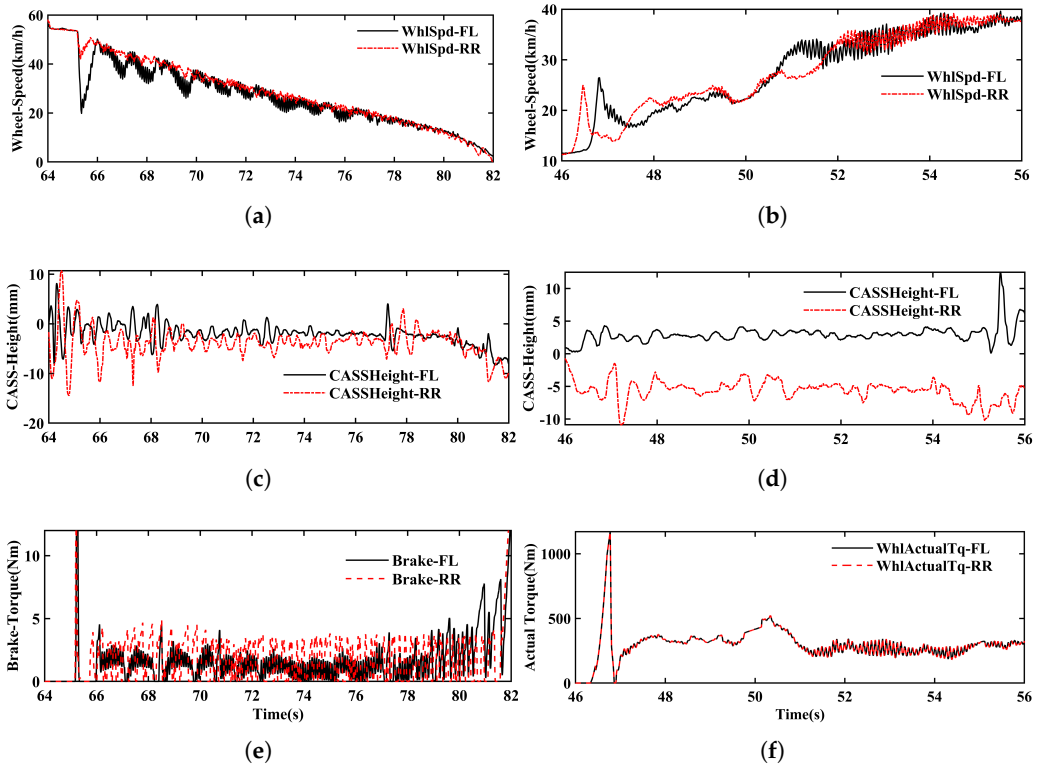


Figure 7. Experimental results of high-frequency wheel oscillation observed during ABS and TCS operation on simulated low-adhesion surfaces: (**a**) wheel speed during braking; (**b**) wheel speed during traction (TCS intervention); (**c**) suspension vertical displacement during braking; (**d**) suspension vertical displacement during traction; (**e**) braking torque during ABS intervention; (**f**) driving torque during TCS intervention.

5. Experiments and Discussions

To validate the effectiveness of the proposed method, both the ABIFR and MP-LC algorithm were deployed on the main controller. Experiments were conducted using the M917 test vehicle under both simulated low-adhesion conditions (with a friction coefficient of approximately $\mu = 0.1$) and high-adhesion conditions (dry asphalt with a friction coefficient of $\mu = 0.9$). The acceleration measurement accuracy is 0.01 m/s², the wheel speed accuracy is 0.0025 m/s, and the brake force output accuracy is 1 N, with a sampling period of 5 ms. Three sets of comparative tests were performed: Group 1 employed a conventional ABS strategy; Group 2 integrated the ABIFR method; Group 3 combined both the ABIFR and MP-LC control strategies.

As shown in Figure 8, the test results under low-adhesion braking conditions for the conventional ABS strategy are illustrated in Figure 8a,d,g, representing wheel speed, braking force, and longitudinal deceleration, respectively. Braking is initiated at 37.5 s, triggering the ABS system. Under such conditions, each torque reduction cycle in conventional ABS reduces the braking torque to nearly zero, resulting in slightly lower braking force—approximately in the range of 0–5000 N, but with no apparent high-frequency oscillation.

After integrating the ABIFR strategy, the torque reduction is no longer to zero but is moderately attenuated, as shown in Figure 8e. However, this introduces high-frequency oscillations in the wheel speed, as evident in Figure 8b where the right rear wheel exhibits periodic fluctuations at around 80 ms intervals. This leads to noticeable discomfort for the driver. The corresponding deceleration, shown in Figure 8h, also demonstrates increased oscillatory behavior. When the MP-LC method is additionally incorporated, the high-frequency oscillation is effectively suppressed. As shown in Figure 8c, the wheel

speed becomes smoother, the braking force increases to approximately 0–9000 N, and the longitudinal deceleration is improved, indicating better braking performance and ride comfort.

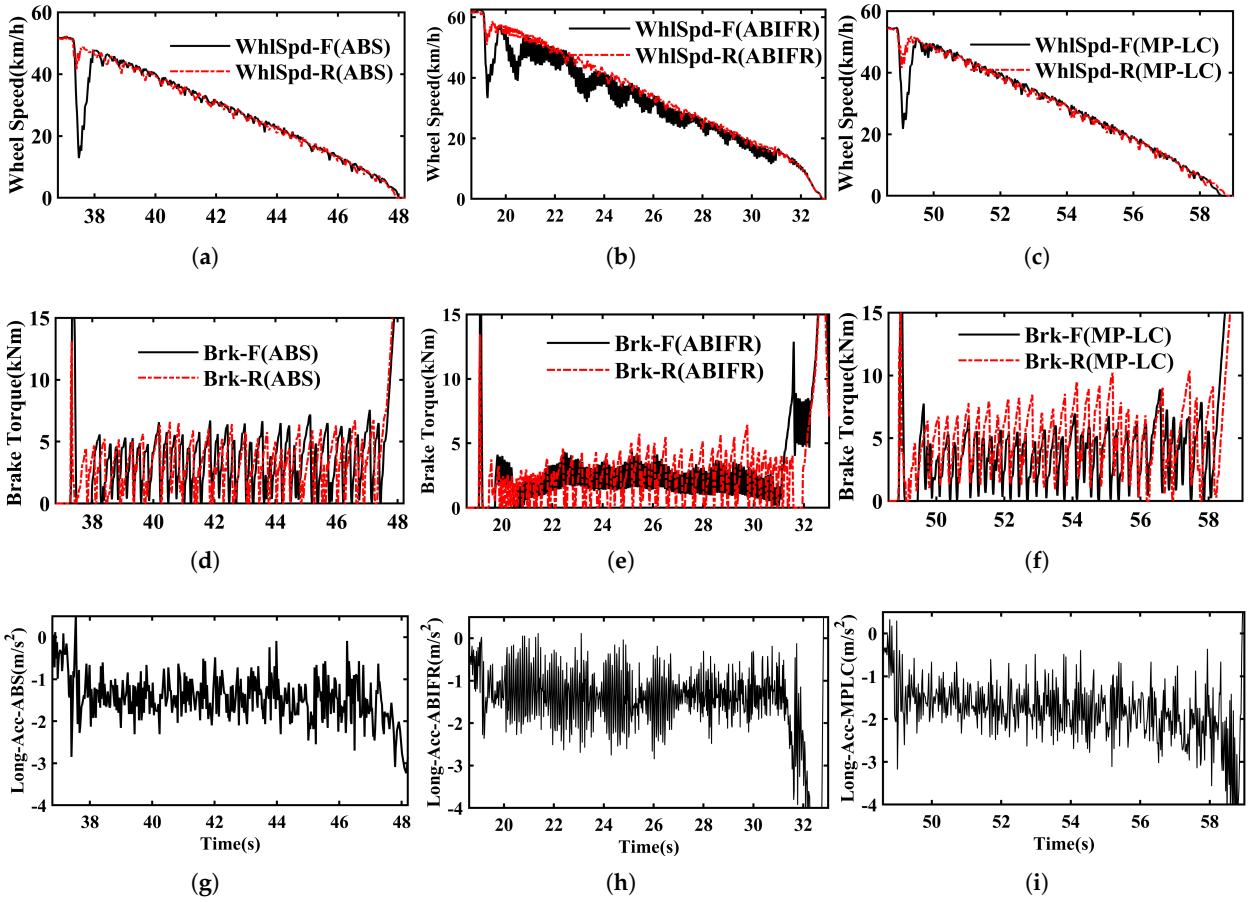


Figure 8. Comparison of test results for standard ABS, ABIFR, and MP-LC strategies on low-adhesion roads: (**a**) wheel speed under conventional ABS; (**b**) wheel speed with ABIFR applied; (**c**) wheel speed with MP-LC applied; (**d**) braking force under conventional ABS; (**e**) braking force with ABIFR applied; (**f**) braking force with MP-LC applied; (**g**) deceleration under conventional ABS; (**h**) deceleration with ABIFR applied; (**i**) deceleration with MP-LC applied.

Under fixed vehicle configuration conditions, the wheel-end oscillation frequency remains approximately 80 ms across various road surfaces, including high-adhesion asphalt, snow, and ice. This consistency allows for the inherent frequency to be pre-calibrated in advance. Although this phenomenon may not be clearly visible in Figure 8a, extensive experimental data collected in this study confirm its inevitability. For instance, in Figure 9a,d, at 29.7 s and 31.5 s, wheel speed oscillations are observed, accompanied by rapid reductions in braking force occurring three to four times at intervals of approximately 80–85 ms. After applying the proposed optimization method, such frequent braking force reductions are no longer present, and braking force loss is avoided. This clearly indicates that stability is not achieved through passive tire recovery but rather through our active intervention strategy.

The test results are evaluated using the Mean Fully Developed Deceleration (MFDD) metric, which serves as a key indicator of braking performance. MFDD represents the average deceleration achieved during the fully developed braking phase and can be expressed as follows:

$$MFDD = \frac{v_b^2 - v_e^2}{25.92(S_e - S_b)} \tag{29}$$

In this formula

v_0—the initial braking velocity of the test vehicle (km/h);
v_b—the vehicle speed at 80% of the initial speed, i.e., $v_b = 0.8v_0$ (km/h);
v_e—the vehicle speed at 10% of the initial speed, i.e., $v_e = 0.1v_0$ (km/h);
S_b—the distance traveled by the vehicle while decelerating from v_0 to v_b (m);
S_e—the distance traveled by the vehicle while decelerating from v_0 to v_e (m).

Additionally, the longitudinal acceleration measured by the IMU over a period of time was used as a reference. However, this signal exhibited significant fluctuations and was affected by the vehicle's pitch angle, thus serving only as a supplementary indicator. As shown in Table 2 under standard ABS conditions, the MFDD was measured at -1.27 m/s^2. After introducing the ABIFR strategy, the MFDD decreased to -1.12 m/s^2, representing an 11.8% reduction. With the implementation of the MP-LC strategy, the MFDD increased to -1.45 m/s^2, representing a 14.2% improvement compared to the baseline ABS condition. The Root Mean Square Error (RMSE) of the longitudinal acceleration, which reflects the fluctuation level of deceleration, increased to 0.72 under ABIFR due to high-frequency oscillations. After implementing the MP-LC strategy, the RMSE value was reduced to 0.52, indicating that the proposed method not only improved the average deceleration level but also significantly suppressed the deceleration fluctuations.

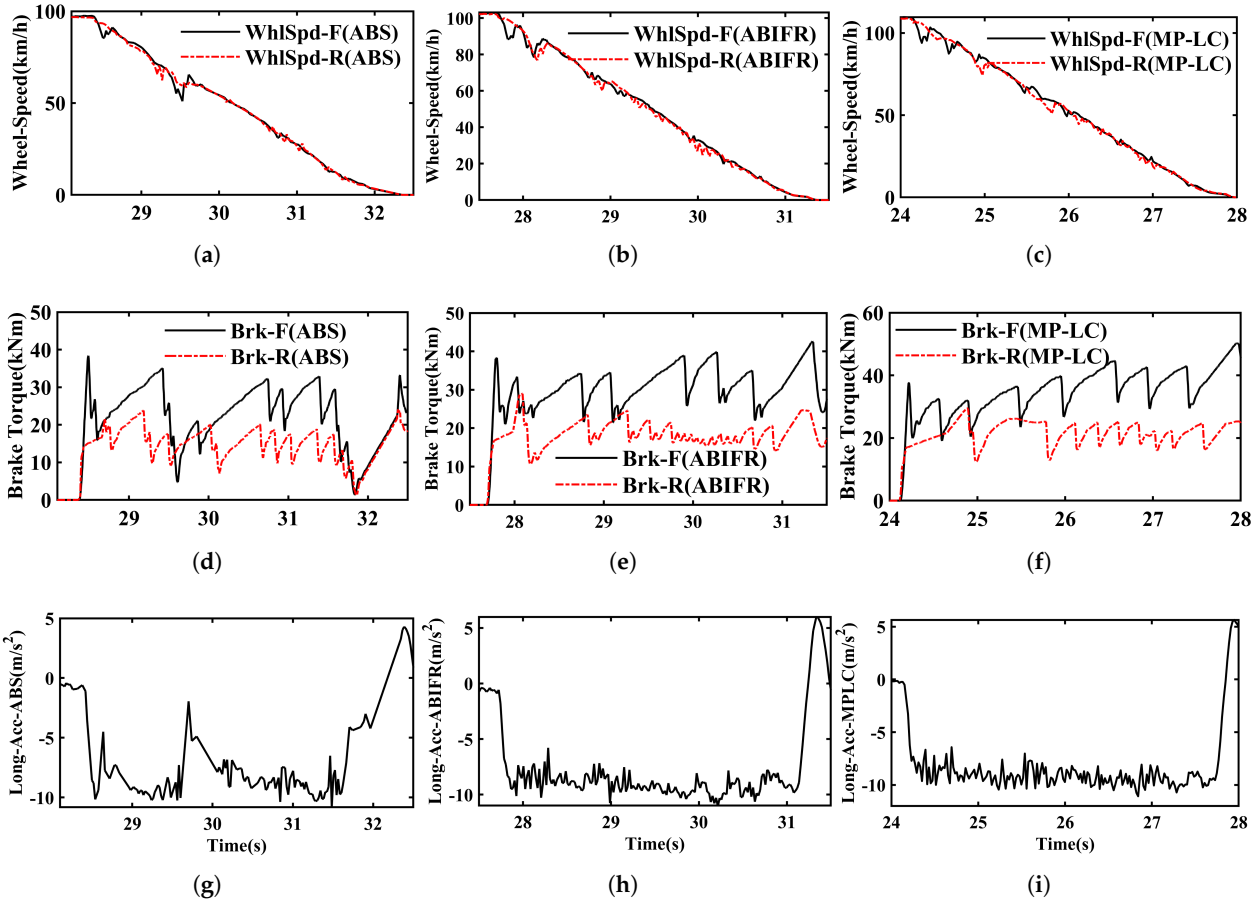


Figure 9. Comparison of test results for standard ABS, ABIFR, and MP-LC strategies on high-adhesion roads: (**a**) wheel speed under conventional ABS; (**b**) wheel speed with ABIFR applied; (**c**) wheel speed with MP-LC applied; (**d**) braking force under conventional ABS; (**e**) braking force with ABIFR applied; (**f**) braking force with MP-LC applied; (**g**) deceleration under conventional ABS; (**h**) deceleration with ABIFR applied; (**i**) deceleration with MP-LC applied.

Similar issues can also occur under high-adhesion conditions when the driver performs rapid acceleration or emergency braking maneuvers, such as during ABS operations. Subjectively, drivers often perceive intense vibrations at the wheels, while objective measurements reveal periodic oscillations at specific frequencies in the wheel speed signals, indicating the presence of inherent resonant modes within the system.

The corresponding test results are summarized in Table 2.

Table 2. Comparison of test results of three cases: ordinary ABS, ABIFR, and MP-LC.

Measurement	MFDD (m/s^2)	Mean Acceleration (m/s^2)	RMSE (m/s^2)
Low μ ABS	−1.27	−1.47	0.45
Low μ ABIFR	−1.12	−1.46	0.72
Low μ MP-LC	−1.45	−1.79	0.52
High μ ABS	−7.46	−7.46	3.68
High μ ABIFR	−8.38	−9.09	0.85
High μ MP-LC	−8.61	−9.23	0.80

In Figure 9b,e, the rear wheels of the vehicle exhibit fixed-frequency oscillations during high-adhesion braking, with both wheel speed and braking force showing periodic fluctuations with a cycle of 80 ms, corresponding to a frequency of 12.5 Hz.

This type of oscillation is not prominent under conventional ABS control but can lead to more severe consequences. The frequent wheel speed fluctuations cause the ABS to misinterpret wheel recovery followed by re-locking, thereby triggering repeated torque reductions. These frequent reductions in braking force significantly degrade braking performance. As shown in Figure 9a,d, after the front wheel speed drops at 29.5 s, it briefly rises and then drops again, resulting in abnormal fluctuations. This triggers three consecutive ABS torque reductions, decreasing the braking force to approximately 4 kN. A similar scenario occurs at 31.6 s, with the braking force dropping to around 2 kN, leading to a substantial loss in braking effectiveness. After integrating the ABIFR and MP-LC strategies, as illustrated in Figure 9c,f, the wheel speed and braking force exhibit more stable and regular patterns. Moreover, the longitudinal deceleration shown in Figure 9i becomes smoother and significantly higher.

A comparison of the three methods, as presented in Table 2, shows that under conventional ABS control, the MFDD is limited to $-7.46\ m/s^2$ due to frequent braking force loss. After introducing the ABIFR strategy, MFDD improves to $-8.38\ m/s^2$. With the additional integration of the MP-LC method, MFDD further increases to $-8.61\ m/s^2$, representing a 15.4% improvement over standard ABS. Moreover, the RMSE is reduced, indicating diminished fluctuation in deceleration and enhanced braking stability. In practical applications, the control performance and braking distance can be further improved through calibration procedures and the application of correction coefficients.

6. Conclusions

This study investigates the high-frequency wheel vibration phenomenon observed in DDEV, particularly under ABS operation on low-adhesion surfaces. A single-wheel dynamic model incorporating vehicle body mass, wheel mass, suspension, tire stiffness, and damping is established. Modal and frequency domain analyses reveal that the root cause of wheel speed oscillation is circumferential resonance induced by the elastic coupling between the motor and tire, rather than vertical vibrations. Simulation results indicate that tire resonance typically occurs in the 12–13 Hz range, which aligns well with experimental observations. To address this issue, an ABIFR strategy and an MP-LC scheme are proposed. These methods aim to maintain optimal slip ratios and suppress unnecessary torque

reductions, thereby enhancing braking smoothness and overall performance. Experimental validation demonstrates that the proposed methods improve the MFDD by 14.8% and 15.2% under low- and high-adhesion conditions, respectively, while effectively eliminating the 12–13 Hz high-frequency oscillations. Moreover, the ABS control period is restored to a normal 300 ms, improving overall driving comfort.

Future work will focus on integrating real-time sensor data with model-based predictive control, adapting the approach to different tire and motor configurations, and conducting extensive testing across diverse road and environmental conditions to enhance robustness.

Author Contributions: Conceptualization, Y.X.; methodology, Y.X. and X.W.; software, Z.Z.; validation, L.L., H.W. and Z.L.; formal analysis, Y.X.; investigation, Y.X.; resources, Y.X.; data curation, Y.X.; writing—original draft preparation, Y.X.; writing—review and editing, H.W.; visualization, Y.X.; supervision, X.W.; project administration, L.L.; funding acquisition, X.W. All authors have read and agreed to the published version of the manuscript.

Funding: This research was funded by the National Natural Science Foundation of China (Grant No. 52472412, Grant No. 52402477) and the Shandong Provincial Key Research and Development Program (Grant No. 2023CXGC010214).

Data Availability Statement: The data that support the findings of this study are available from the corresponding authors upon reasonable request.

Acknowledgments: The authors would like to express their sincere gratitude to Dongfeng R&D Institute for providing the M917 and Eπ007 vehicles used in this study. Appreciation is also extended to Trinova Intelligent Technology for offering the experimental test site. Special thanks are extended to Cheng Li, Kunpeng Jiang, Chen Zhang, Linxi Li, Zhixin Yang, Meng'en Ma, and Zeyuan Chu from Ocean University of China for their valuable contributions to data collection during the experiments. All scientific content, analyses, conclusions, and references were independently created, verified, and approved by the authors. ChatGPT-4.0 (OpenAI, 2025) was used solely to assist with language polishing, grammar correction, and preliminary literature summary.

Conflicts of Interest: Authors Yinggang Xu, Zheng Zhu, Zhaonan Li, and Heng Wei are Ph.D. candidates at Tsinghua University. Xiangyu Wang and Liang Li are faculty members at Tsinghua University. The research and experiments presented in this paper are part of a collaborative project between Tsinghua University and Dongfeng Motor Corporation R&D Institute, focusing on the development and validation of a skateboard chassis platform. The remaining authors declare that the research was conducted in the absence of any commercial or financial relationships that could be construed as potential conflicts of interest.

References

1. Wu, T.; Li, J.; Qin, X. Braking performance oriented multi-objective optimal design of electro-mechanical brake parameters. *PLoS ONE* **2023**, *16*, e0251714. [CrossRef]
2. Shi, P.; Min, Y.; Wang, H.; Lv, L. Dynamic Simulation of Ground Braking Force Control Based on Fuzzy Adaptive PID for Integrated ABS-RBS System with Slip Ratio Consideration. *World Electr. Veh. J* **2025**, *16*, 372. [CrossRef]
3. Li, C.; Zhuo, G.; Tang, C.; Xiong, L.; Tian, W.; Qiao, L.; Duan, Y. A review of electro-mechanical brake (EMB) system: Structure, control and application. *Sustainability* **2023**, *15*, 4514. [CrossRef]
4. Megna, G.; Bracciali, A. Tread-Braked Wheels: Review and Recent Findings. *Machines* **2025**, *13*, 579. [CrossRef]
5. Sun, W.; Li, Y.; Huang, J.;Zhang, N. Vibration effect and control of in-wheel switched reluctance motor for electric vehicle. *J. Sound Vib.* **2015**, *338*, 105–120. [CrossRef]
6. Koylu, H.; Cinar, A. Dynamical investigation of effects of variable damper settings induced brake pressure oscillations on axle and wheel oscillations during ABS-braking based on experimental study. *Meccanica* **2013**, *48*, 1093–1115. [CrossRef]
7. Luo, Y.; Tan, D. Study on the dynamics of the in-wheel motor system. *IEEE Trans. Veh. Technol.* **2012**, *61*, 3510–3518. [CrossRef]
8. Podrigalo, M.; Klets, D.; Sergiyenko, O.; Gritsuk, I. V.; Soloviov, O.; Tarasov, Y.; Bilousova, T. Improvement of the assessment methods for the braking dynamics with abs malfunction. In *SAE Technical Paper 2018-01-1881*; SAE: Warrendale, PA, USA, 2018.

9. Bayar, K. Active motor damping strategy for driveline vibrations of a hybrid electric vehicle during ABS operation. *Part D J. Automob. Eng.* **2023**, *237*, 2499–2510. [CrossRef]
10. Ciupe, V.; Mărgineanu, D.; Lovasz, E.-C. Scaled test stand simulation for studying the behavior of anti-lock brake systems on bumpy roads. In *New Advances in Mechanisms, Mechanical Transmissions and Robotics*; Mechanisms and Machine Science; Springer: Cham, Switzerland, 2016.
11. Mayer, S.; Le, H. V.; Nesti, A.; Henze, N.; Bülthoff, H. H.; Chuang, L. L. The effect of road bumps on touch interaction in cars. In Proceedings of the 10th International Conference on Automotive User Interfaces and Interactive Vehicular Applications, Toronto, ON, Canada, 23–25 September 2018.
12. Li, Q.; Wang, X.; Zhang, B.; Li, L.; Pei, Y.; Ping X. Research on tire longitudinal-vertical coupling state observation and slip ratio control under bumpy road. *J. Mech. Eng.* **2021**, *57*, 62–73.
13. Yu, L.; Wang, H.; Song, J.; Qi, X.; Kong, L. Performance evaluation and test of anti-lock braking system hydraulic system. *J. Mech. Eng.* **2007**, *43*, 40–46. [CrossRef]
14. Van der Merwe, N. A.; Els, P.S.; Žuraulis, V. ABS braking on rough terrain. *J. Terramech.* **2018**, *80*, 49–57. [CrossRef]
15. Zhao, Z.; Taghavifar, H.; Du, H.; Qin, Y.; Dong, M.; Gu, L. In-wheel motor vibration control for distributed-driven electric vehicles: A review. *IEEE Trans. Transp. Electrif.* **2021**, *7*, 2864–2880. [CrossRef]
16. Mao, Y.; Zuo, S.; Wu, X.; Duan, X. High frequency vibration characteristics of electric wheel system under in-wheel motor torque ripple. *J. Sound Vib.* **2017**, *400*, 442–456. [CrossRef]
17. Ghosh, A.; Chatterjee, S. An overview on various sources of vibration in electric vehicle and their identification techniques. *J Braz. Soc. Mech. Sci. Eng.* **2023**, *45*, 401. [CrossRef]
18. Zuo, L.; Nayfeh, S.A. Structured H2 optimization of vehicle suspensions based on multi-wheel models. *Veh. Syst. Dyn.* **2023**, *40*, 351–371. [CrossRef]
19. Qin, Y.; Rath, J.J.; Hu, C.; Sentouh, C.; Wang, R. Adaptive nonlinear active suspension control based on a robust road classifier with a modified super-twisting algorithm. *Nonlinear Dyn.* **2019**, *97*, 2425–2442. [CrossRef]
20. Wang, W.; Li, G.; Song, Y. Nonlinear dynamic analysis of the whole vehicle on bumpy road. *Trans. Tianjin Univ.* **2010**, *16*, 50–55. [CrossRef]
21. Wilson, G.N.; Ramirez-Serrano, A.; Sun, Q. Geometric-based tyre vertical force estimation and stiffness parameterisation for automotive and unmanned vehicle applications. *Veh. Syst. Dyn.* **2017**, *55*, 168–190. [CrossRef]
22. Wen, S.; Chen, M.Z.; Zeng, Z.; Yu, X.; Huang, T. Fuzzy control for uncertain vehicle active suspension systems via dynamic sliding-mode approach. *IEEE Trans. Syst.* **2016**, *47*, 24–32. [CrossRef]
23. Yang, Y.; Liu, C.; Chen, L.; Zhang, X. Phase deviation of semi-active suspension control and its compensation with inertial suspension. *Acta Mech. Sin.* **2024**, *40*, 523367. [CrossRef]
24. Tan, D.; Song, F.; Wang, Q. Design and optimization of the in-wheel motor driving electric vehicle based on the vibration energy transmission. *J. Vib. Control* **2018**, *24*, 5129–5140. [CrossRef]
25. Meléndez-Useros, M.; Jiménez-Salas, M.; Viadero-Monasterio, F.; Boada, B.L. Tire Slip H∞ Control for Optimal Braking Depending on Road Condition. *Sensors* **2023**, *23*, 1417. [CrossRef]
26. Nguyen, D.N.; Nguyen, T. A. The dynamic model and control algorithm for the active suspension system. *Math. Probl. Eng.* **2023**, *2023*, 2889435. [CrossRef]
27. Suman, S.; Balaji, P.S.; Selvakumar, K.; Kumaraswamidhas, L.A. Nonlinear vibration control device for a vehicle suspension using negative stiffness mechanism. *J. Vib. Eng. Technol.* **2021**, *9*, 957–966. [CrossRef]
28. Lopes, R.; Farahani, B.V.; Queirós de Melo, F.; Moreira, P.M.G.P. A Dynamic Response Analysis of Vehicle Suspension System. *Appl. Sci.* **2023**, *13*, 2127. [CrossRef]
29. He, Z.; Shi, Q., Wei, Y.; Gao, B.; Zhu, B.; He, L. A model predictive control approach with slip ratio estimation for electric motor antilock braking of battery electric vehicle. *IEEE Trans. Ind. Electron.* **2021**, *69*, 9225–9234. [CrossRef]
30. Duda, K.; Marszalek, Z. Vehicle speed determination with inductive-loop technology and fast and accurate fractional time delay estimation by DFT. *Metrol. Meas. Syst.* **2024**, *31*, 781–796. [CrossRef]
31. Haralick, R. M.; Zhuang, X.; Lin, C.; Lee, J. S. The digital morphological sampling theorem. *IEEE Trans. Acoust. Speech Signal Process.* **2002**, *37*, 2067–2090. [CrossRef]
32. Cheng, S.; Li, L.; Guo, H. Q.; Chen, Z. G.; Song, P. Longitudinal collision avoidance and lateral stability adaptive control system based on MPC of autonomous vehicles. *IEEE Trans. Intell. Transp. Syst.* **2019** ,*21*, 2376–2385. [CrossRef]

Disclaimer/Publisher's Note: The statements, opinions and data contained in all publications are solely those of the individual author(s) and contributor(s) and not of MDPI and/or the editor(s). MDPI and/or the editor(s) disclaim responsibility for any injury to people or property resulting from any ideas, methods, instructions or products referred to in the content.